Gating of Substrate Access and Long-Range Proton Transfer in Escherichia coli Nitrate Reductase A: The Essential Role of a Remote Glutamate Residue

Sinan Al-Attar, Julia Rendon, Marlon Sidore, Jean-Pierre Duneau, Farida Seduk, Frédéric Biaso, Stéphane Grimaldi, Bruno Guigliarelli, Axel Magalon

To cite this version:

Sinan Al-Attar, Julia Rendon, Marlon Sidore, Jean-Pierre Duneau, Farida Seduk, et al.. Gating of Substrate Access and Long-Range Proton Transfer in Escherichia coli Nitrate Reductase A: The Essential Role of a Remote Glutamate Residue. ACS Catalysis, 2021, 11 (23), pp.14303-14318. 10.1021/acscatal.1c03988 . hal-03511729

HAL Id: hal-03511729
https://amu.hal.science/hal-03511729v1

Submitted on 5 Jan 2022

Gating of substrate access and long-range proton transfer in *Escherichia coli* nitrate reductase A: the essential role of a remote glutamate residue

Sinan Al-Attar[1], Julia Rendon[2‡], Marlon Sidore[3‡], Jean-Pierre Duneau[3], Farida Seduk[1], Frédéric Biaso[2], Stéphane Grimaldi[2], Bruno Guigliarelli[2*] and Axel Magalon[1*]

1 : Aix Marseille Université, CNRS, Laboratoire de Chimie Bactérienne (UMR7283), IMM, IM2B, 13402 Marseille, France
2 : Aix Marseille Université, CNRS, Laboratoire de Bioénergétique et Ingénierie des Protéines (UMR7281), IMM, IM2B, 13402 Marseille, France
3 : Aix Marseille Université, CNRS, Laboratoire d'Ingénierie des Systèmes Macromoléculaires (UMR7255), IMM, IM2B, 13402 Marseille, France

‡ Both authors contributed equally to the work
*Corresponding authors: Dr. Axel Magalon, Aix Marseille Université, CNRS, Laboratoire de Chimie Bactérienne (UMR7283), IMM, IM2B, 13402 Marseille, France, magalon@imm.cnrs.fr tel : +33 491164668 and Prof. Bruno Guigliarelli, Aix Marseille Université, CNRS, Laboratoire de Bioénergétique et Ingénierie des Protéines (UMR7281), IMM, IM2B, 13402 Marseille, France, guigliar@imm.cnrs.fr tel : +33 491164567

Abstract

The Mo/W-*bis*PGD enzyme superfamily comprises a vast number of mononuclear molybdenum and tungsten enzymes that catalyze a great diversity of vital reactions in prokaryotes. In the past decades, much attention has been devoted to the immediate surroundings of the metal atom highlighting the importance of the inner coordination sphere but have failed to identify molecular determinants of the reactivity. Here, we report the mechanistic importance of a set of conserved residues that line the substrate entry tunnel in *Escherichia coli* nitrate reductase A (Nar), a paradigmatic enzyme of the Mo/W-*bis*PGD superfamily. Using mutagenesis, enzyme kinetics, electron paramagnetic resonance spectroscopy and molecular dynamics, we unveil the pivotal role of Glu-581 motion and a number of polar residues in its close proximity in substrate affinity and proton transfer to the Mo active site. Motion of the side chain of Glu-581 exhibiting a strong acid-base cooperativity with Asp-801 and surrounded by several polar interactions controls the hydration inside the protein core, proton transfer and substrate selectivity towards the active site. Overall, we identify an additional determinant that fine-tunes the reactivity and selectivity in Nar and propose that a gating mechanism is at play in several other members of the superfamily.

Keywords: nitrate reductase, molybdenum, molybdenum enzyme, gating, molybdopterin.

Introduction

Among the mononuclear Mo-enzymes, the Mo/W-*bis*PGD superfamily is by far the most diverse in terms of cofactor composition, substrate and type of catalyzed chemical reactions (1, 2). While most members in this superfamily catalyze oxygen atom transfer reactions, others catalyze sulfur or hydrogen atom transfer, or even non-redox reactions. The Mo/W-*bis*PGD enzyme superfamily is widespread among prokaryotes and is represented by vital enzymes that are mostly involved in metabolic pathways. Furthermore, phylogenetic and paleogeochemistry studies indicated that several members were likely present in the first forms of life on Earth (3, 4). The Mo/W atom is covalently bound to four thiolates originating from two pyranopterins substituted by a guanosine moiety. The hexavalent coordination shell of the metal is completed by an amino acid ligand (aspartate, serine or (Se)cysteine) and an inorganic sulfur or oxygen atom, with the exception of arsenite oxidase having no amino acid ligand (5, 6). Overall, a conundrum exists in this enzyme superfamily when considering the limited chemical diversity of Mo/W active sites and a yet uncovered diversity of reactivities and substrates (1, 2, 5, 7).

Recent studies have started to untangle this conundrum by demonstrating the participation of the hydrogen-bond network surrounding the pterin moieties in modulating the redox chemistry at the Mo center (8, 9). While being informative, these studies call for exploration of the environment surrounding the Mo center since the molecular determinants responsible for fine-tuning the reactivity of the Mo/W active site remain largely unknown. Here, nitrate reductase A (Nar) from *Escherichia coli* can be considered as a good representative model enzyme for the Mo/W-*bis*PGD superfamily owing to its prototypical fold and the cofactor composition of its catalytic subunit, NarG, which contains the Mo cofactor and one Fe_4S_4 cluster referred to as FS0 (10-12). From an evolutionary point of view, Nar is one of the few Mo/W-*bis*PGD enzymes that were proposed to have been present in LUCA (3, 13). Phylogenetic analysis places Nar in a major clade sharing Asp/Oxygen as Mo coordinating ligands (1, 14) together with ethylbenzene dehydrogenase and perchlorate reductase (Pcr) for which X-ray structural data are also available (15, 16). Moreover, Nar is an attractive model due to its high stability, oxygen insensitivity and the wealth of biochemical, spectroscopic and structural data available on the enzyme (10, 17-21). During turnover, the Mo cofactor is considered to cycle between Mo(IV), Mo(V) and Mo(VI) states (5, 22) and two distinct pH-dependent Mo(V) electron paramagnetic resonance (EPR) signatures designated as “low pH” and “high pH” have been identified in Nar (19, 23-25). However, the relationship between these two species and the structures of the Mo center proposed by crystallographic studies is still unclear. A recent study, combining the use of continuous wave and pulsed EPR techniques with structure-based DFT calculations, led to the first description of a structural model for the low pH Mo(V) species involving coordination of the metal by a monodentate ligand Asp222 and a hydroxo group (21). While the currently proposed mechanism for the catalytic cycle of Nar implies a direct transfer of an oxygen atom from the substrate to the metal (5, 22), a more detailed description of the cycle can be proposed by including the structure of the Mo(V) species and the possible switch of the aspartate ligand from monodentate to bidentate coordination as suggested by Pcr structures and mutagenesis studies (16) (Fig. 1). However, these mechanistic details still need to be confirmed and crystal structures in the presence of either the substrate or the product or in other redox states are still lacking.

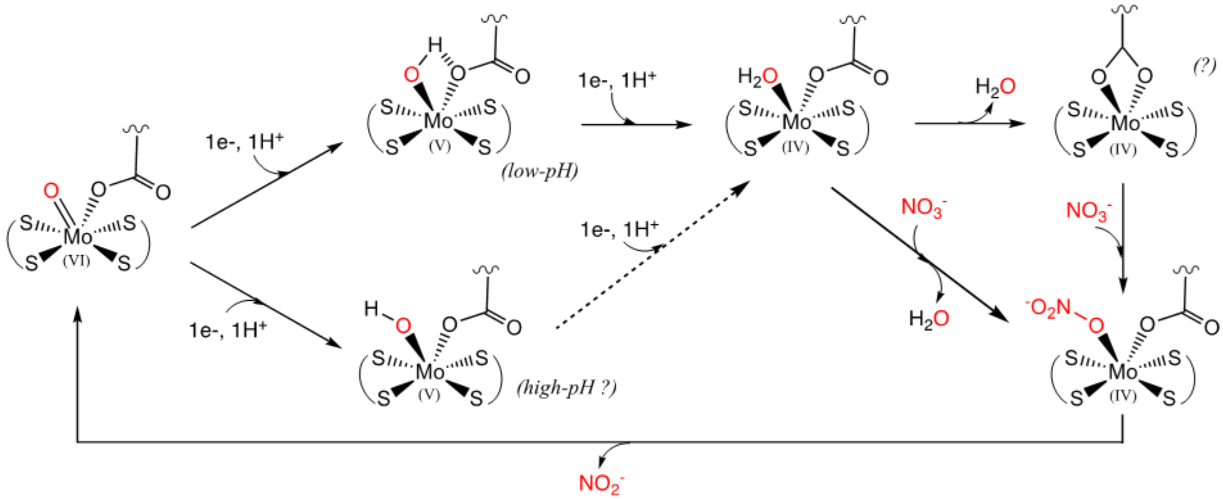

Figure 1: Proposed catalytic scheme for nitrate reduction by the respiratory nitrate reductase NarGH. The atoms originating from the nitrate substrate are indicated in red. The structure of the Mo(V) species at high pH is still hypothetical as well as its involvement in the catalysis. This scheme includes the possible switch in aspartate coordination as proposed for the catalytic mechanism of Pcr (16).

While the precise catalytic role of the high and low pH species remains to be elucidated and especially within the context of proton transfer, their interconversion is likely to be strongly influenced by the H-bond network around the Mo cofactor rather than by a simple acid-base equilibrium (20).

As recognized in all structures of Mo/W-*bis*PGD enzymes, the deeply buried Mo/W active site is connected to the bulk by a tunnel postulated to control substrate access on the basis of various sterical and physico-chemical properties (10, 11, 15, 16, 26-37). A buried active site can be a means to control substrate specificity (38, 39), to create a suitable environment for specific chemical reactions by controlling solvent access to the active site (40, 41) and/or to influence the redox potential of the metal site through controlling the dielectric constant of the environment (42). Furthermore, it has been established that the amino acid composition and structural dynamics of such substrate tunnels can be important factors that influence the reactivity of an enzyme (43-45).

By combining site-directed mutagenesis with detailed kinetic and EPR studies, we have identified a set of strictly conserved amino acid residues in NarG located at the bottleneck of the tunnel and at a remote distance from the Mo active site. Supported by molecular dynamics, this work has shed light on the pivotal role of Glu-581 and a number of polar residues in its close proximity in substrate affinity and proton transfer to the Mo active site likely via the stabilization of a water tunnel.

Materials and Methods

Structural analysis. The substrate tunnel in Nar was mapped using the Caver 3.0 plugin tool for PyMOL (46) employing the default modeling parameters but using a probe size of between 0.8 and 1.2 Å. The structure images were created using PyMOL (DeLano Scientific LLC)

Site-directed mutagenesis. NarGH variants were generated using the overlap-extension PCR method with $pNarGH_{His6}J$ as template (47). For the cloning of the DNA fragment containing the Glu-581 and Tyr-217 variants, the restriction sites SacI and XagI were utilized. The Asp-801 mutant fragments were cloned using SacI and NsiI restriction sites (See Table S1 for primer sequences). PrimeStar high-fidelity DNA polymerase (Takara) was used for all amplification steps. Restriction enzymes were purchased from Invitrogen. T4 DNA ligase was from Promega. Purification kits for PCR products and DNA extraction from gel were from Thermo Scientific. The PCR-amplified sequences were verified by Sanger sequencing (GATC Biotech, Germany).

Protein expression and purification. The Wild-Type (WT) and NarGH variants were overproduced in the nitrate reductase-deficient JCB4023 *E. coli* strain using the pNarGH$_{His6}$J plasmid (47). For kinetics measurements, protein production was performed in LB medium supplemented with 5 µM of sodium molybdate. For the production of ^{98}Mo-enriched NarGH, the growth was performed in M9 minimal medium (47) supplemented with 5 µM $Na^{98}MoO_4$ (Oak Ridge National Laboratory, USA). Protein production and purification were carried-out as described earlier (47) using nickel affinity chromatography and proteins were dialyzed in a buffer containing 100 mM MOPS (pH 7,5) and 1 mM EDTA. Protein concentrations were determined using the Lowry method (48). Molybdenum content analysis of purified WT and NarGH variants was performed using inductively coupled plasma mass spectrometry (ICP-MS) as described before (49).

Enzymatic activity assays. Steady-state kinetics were performed at room temperature (24 ± 1 ˚C) in a N_2-filled anaerobic glovebox (Jacomex, $[O_2] < 2$ ppm) using dithionite-reduced benzyl viologen (Sigma) as artificial electron donor (0.2 mM) and NO_3^- or ClO_3^- as electron acceptors (50, 51). Reduced bipyridylium compounds (benzyl viologen or methyl viologen) are classically used as electron donor of choice for molybdenum-containing enzymes. Although they are artificial compounds, the $K_m^{nitrate}$ calculated using reduced BV on the soluble NarGH complex in this study and in (51) is of the same order of magnitude as that obtained using reduced menaquinone analogs on the membrane-associated NarGHI complex (52). We can therefore assert with high confidence that the use of an artificial electron donor like BV is unlikely to have an impact on substrate recognition. The activity was followed by measuring oxidation of benzyl viologen spectrophotometrically at 600 nm ($\varepsilon_{600,\,BV} = 7.0945$ mM^{-1}cm^{-1}) (Safas Monaco spectrophotometer). Measurements were started by addition of nitrate or chlorate to a solution containing the enzyme and reduced BV, and the reaction was monitored for 5 minutes. The rate of the BV oxidation was corrected by subtracting the slope occurring without substrate. All measurements were done using a mixed buffer composed of CAPS, MES, CHES and HEPES, each component at a concentration of 20 mM. The effect of the pH on the kinetic parameters was systematically determined for all the variants except for E581Q and Y217F/D801L due to their strongly diminished activity. Each measurement was performed at least three times with independent protein purifications.

The kinetic parameters (k_{cat}, $K_m^{nitrate}$ and $K_m^{chlorate}$) were obtained by fitting the initial benzyl viologen oxidation rates as function of nitrate or chlorate concentration with the *Michaelis-Menten* equation. Although the *Michaelis constant*, K_m, is not a thermodynamic binding constant, in the case where two enzymes have similar k_{cat} values, a strong variation of their K_m values can be interpreted as changes in affinity for the substrate. The catalytic constants k_{cat} were calculated in respect to one catalytically active protomer NarGH (molecular mass = 198 kDa). The pH profiles of the k_{cat} and K_m of each tested variant were fitted using Eq. 1 or a modified form of it depending on how many pK_a values are fitted. For example, Eq. 1 accounts for a situation where the K_m evolution as function of pH increases then decreases. Herein A_{max} is the maximal k_{cat} or K_m simulated and pK_n (n = 1 or 2) denotes a pK_a value.

$$A(pH) = \frac{A_{max}}{1+10^{pK_1-pH}} - \frac{A_{max}}{1+10^{pK_2-pH}} \qquad \text{Eq. 1}$$

Eq. 2 was used to calculate the differences in transition-state energies ($\Delta\Delta G_{ES}^{\ddagger}$) between the WT and the variants or between two substrates with the same variant (53). The superscript $\ddagger$ denotes the transition state. The parameters used for the calculation were from the measurements at pH 6.5.

$$\Delta\Delta G_{ES^{\ddagger}} = -RTln\left[\frac{\left(\frac{k_{cat}^{A}}{K_{M}^{A}}\right)}{\left(\frac{k_{cat}^{B}}{K_{M}^{B}}\right)}\right]$$

Eq. 2

Here, the superscripts *A* and *B* denote WT and variants, respectively, when one is interested in the change in transition-state energy due to the introduction of a substitution. If the aim is to calculate the energy change concerned with the change of substrate, then A and B represent nitrate and chlorate, respectively. A negative outcome indicates that the transition-state energy has increased and *vice versa*.

Redox potentiometry and electron paramagnetic resonance (EPR) spectroscopy. Redox titration experiments were performed in an anaerobic glove-box (Jacomex, $[O_2] < 2$ ppm) at room temperature in titration buffer (50 mM MOPS, 25 mM Bicine, 1 mM EDTA, pH 7.5) containing 10 µM of the following redox mediators: N,N,dimethyl-p-phenylenediamine; 1,4-benzoquinone; 2,6-dichlorophenolindophenol; 2,5-dimethyl-p-benzoquinone; 1,2-naphtoquinone; phenazine methosulfate; phenazine ethosulfate; methylene blue; resorufin; and indigo carmine. Reduction and oxidation steps were performed by injecting small volumes of solutions of 10 mM sodium dithionite or 100 mM potassium ferricyanide, respectively and the potentials were measured with a combined Pt-Ag/AgCl/KCl (3M) microelectrode. Redox-poised aliquots were transferred into quartz EPR tubes that were frozen inside the glovebox, and subsequently stored in liquid nitrogen prior to EPR experiments. All redox potentials in the text are given with respect to the standard hydrogen electrode (SHE). X-band EPR spectra were recorded using a Bruker-Biospin EleXsys E500 spectrometer equipped with a standard rectangular Bruker EPR cavity (ST 4102) fitted to an Oxford Instruments helium flow cryostat (ESR900). The total Mo(V) content in the samples was quantified relative to the Fe_3S_4 cluster (FS4) content measured in a fully oxidized sample using double integration of their respective EPR signal as previously described (20). The quantity of each individual Mo(V) species was determined on the basis of its relative proportion to that of the total Mo(V) content inferred from spectral simulation (see hereafter). Plotted against the ambient redox potential, their corresponding spin intensity ratio [Mo(V)]/[FS4] (in %) was fitted to a theoretical curve corresponding to two successive one-electron redox processes:

$$[Mo(V)]\Big/[FS4] = \frac{\mathrm{R_{occ}}}{1+\mathrm{e}^{\alpha(\mathrm{E}-\mathrm{E_1})}+\mathrm{e}^{\alpha(\mathrm{E_2}-\mathrm{E})}}$$

Eq. 3

where α = F/RT. E_1 and E_2 are the midpoint potentials of the n = 1 Mo(VI)/Mo(V) and Mo(V)/Mo(IV) redox couples, respectively, R and F are the molar gas and Faraday constants, respectively, T is the absolute temperature in Kelvin, and $\alpha = 39.18\ V^{-1}$ at 23°C. R_{occ} is the occupancy level of the active site. It corresponds to the fraction of the site occupied by either Mo(VI), Mo(V) or Mo(IV). The midpoint potential of the n = 2 Mo(VI)/Mo(IV) couple, which corresponds to the maximal amount of Mo(V), is $E_m = (E_1 + E_2)/2$.

Simulation of Mo(V) EPR spectra. Simulations of frozen solution EPR spectra were carried out using the Easyspin package (54) (release 5.1.11) that works under MatLab (the MathWorks, Inc., Natik). Experimental magnetic fields were corrected for an offset against a standard with known g-value (weak pitch, g = 2.0028). Mo(V) EPR spectra were then simulated by adding the contribution of one, two or three independent species (Table S2). Anisotropic spectral broadening was considered through unresolved hyperfine couplings (HStrain function) for simulations of Mo(V) spectra. The Hstrain parameters $\Delta_{1,2,3}$ correspond to the full width at half maximum (in MHz) of Gaussian lines along the three g-tensor principal axes. Simulations of the low-pH Mo(V) species were carried out by considering an additional proton hyperfine coupling tensor with principal axes assumed to be collinear to those of the Mo(V) g-tensor.

Molecular Dynamics. The AMBER ff03 force field (55) was used for all the systems, including the original parameters for the protein and the parameters for the FeS clusters and GDP that were extracted and re-implemented from (56) and (57), respectively. Owing to the inherent difficulties to obtain meaningful parameters for the molybdenum cofactor (Mo-*bis*PGD) in all redox states, we focused on the structure of the apomolybdo-NarGHI (PDB ID: 1SIW) with negligible structural differences (RMSD 0.24 Å) with NarGHI (PDB ID: 1Q16) and a comparable resolution between 1.9 and 2.2Å. The fact that the apo structure is strictly compatible (to the experimental precision given by the resolution) with that of the holo structure, rules out the possibility that major structural changes accompany the adaptation of the prosthetic group. The apo structure is thus pertinent for exploring the major conformational landscape accessible by the structures, particularly at sites not directly involved in prosthetic group accommodation. The catalytic subunit of the apomolybdo-NarGHI structure comprises a non-covalently bound GDP in the same position as the guanine nucleotide moiety of one of the PGD molecule in the native complex and the FS0 center. All the resolved water molecules present in the structure of the apomolybdo-NarGHI were included in the starting conformation of the MD simulations. The PROPKA software (58) was used to determine the protonation states of each protonatable amino-acid. The protein was solvated in the center of a TIP3P water filled cubic box of 15 nm^3 while 0.15 mM of NaCl was used with an excess of Na^+ ions to neutralize the global charge of the system. Solvation of the entire system in the water box also resulted in the introduction of additional molecules that fill voids, particularly at the active site cavity.

Molecular dynamics (MD) simulations were performed with GROMACS 5.1.4 (59-62) using Particle Mesh Ewald electrostatics with a real-space Coulomb cutoff of 1.2 nm (63) and a van der Waals interactions cutoff of 1.2 nm with a long-range dispersion correction. The neighbor searching algorithm was updated every 10 steps. The timestep was 2 fs with a modified Berendsen thermostat and a 0.1 ps time constant at a temperature of 300 K (64). For the pressure control, an isotropic Parinello-Rahman barostat was used with a 2 ps time constant and a compressibility of 4.5 10^{-5} bar^{-1} at a pressure of 1 bar (65). After a minimization consisting of 3000 steps of steepest descent, a two-step equilibration procedure was set up, first for stabilizing the temperature for 0.1 ns, and a second for the establishment of the pressure control in an additional 0.5 ns. Two simulations were run for 20 ns and the third one was run for 200 ns. The same starting conditions were used for all three simulations, except that the initial atomic velocities were generated from different random distributions. This change in the early stages of the simulations was sufficient for the exploration of slightly different regions of the accessible conformational space. All the calculations were done using 96 processors on the OCCIGEN supercomputer at the CINES center (Montpellier, France). RMSDs in the range of 2 Å were measured for the whole structure (chain A) along the trajectories of each simulation showing no major reorganization at the level of the quaternary structure (Fig. S1). Moreover, all atoms in a range of 15 Å around Glu-581 showed low atomic fluctuations (about 1.5 Å). After centering and fitting the protein using gmx trjconv tool of GROMACS, the simulations were visualized using VMD (66). The Volmap tool was used to compute the water density maps. Hydrogen bonds were computed using gmx hbond. All the scripts used in this work are available at https://framagit.org/msidore/thesis_energetics_lipids/-/tree/master/Notebooks/Nar under the WTFPL license.

Results

Substrate access to the active site is restricted by a group of conserved polar and acidic residues. Scrutiny of the X-ray structures of Nar from *E. coli* indicates that nitrate needs to traverse a distance of about 25 Å from the solvent to reach the Mo active site through a partially constricted tunnel (Fig. 2). This putative substrate entry tunnel does not reach all the way through to the active site but instead terminates at about 10 Å away from the Mo atom at Glu-581. Glu-581 is strictly conserved in all archaeal and bacterial Nar as well as in n-type nitrite oxidoreductases (nNxr), all of which are clustered in the Mo/W-*bis*PGD clade of enzymes that have Asp as Mo ligand (Fig. S2) (1). In most X-ray structures of Nar from *E. coli*, the side chain of Glu-581 has a relatively high *b*-factor (Fig. 2) suggesting that this residue is dynamic and possibly involved in controlling substrate access. The Mo active site being shielded from the bulk implies that protein motion is important for the substrate to interact with the active site.

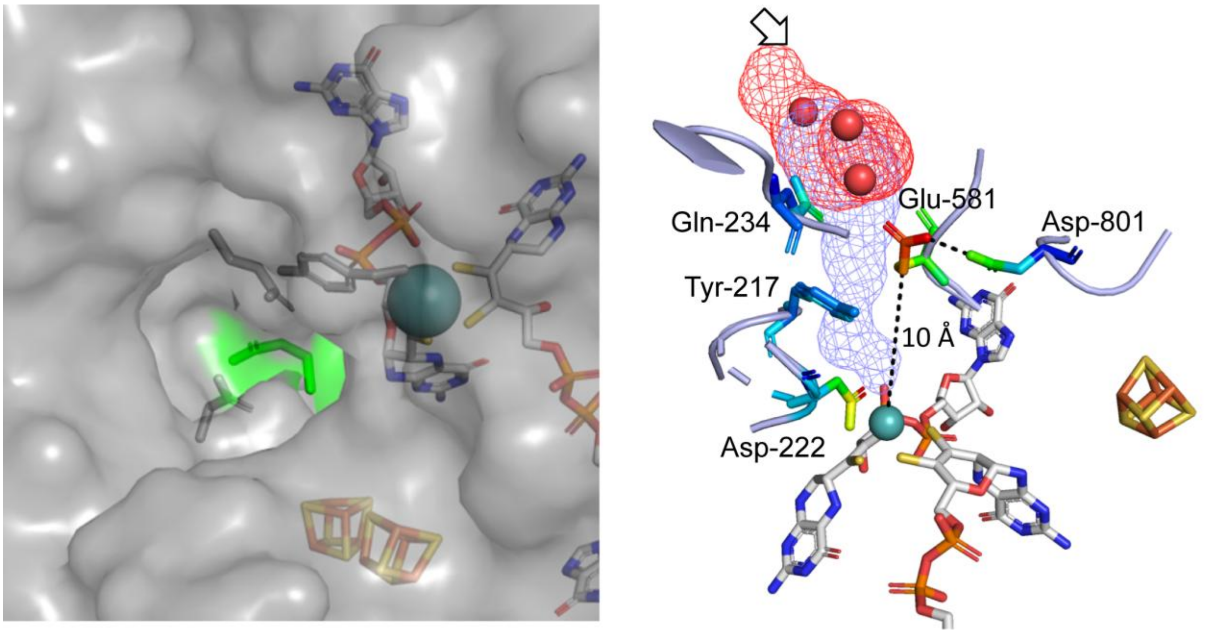

Figure 2. The Mo active site in NarGH is protected from the bulk by the conserved Glu-581. Left: surface representation of NarG (light gray) along with the cofactors showing the location of Glu-581 (green) at the bottom of the substrate tunnel and the proximal polar amino acids. Right: The substrate tunnel (red) is simulated using the Caver tool (with a probe radius of 1.2 Å) showing the bottleneck residue Glu-581 at about 10 Å from the Mo atom while the cavity located immediately above the Mo atom (light blue) involved a probe radius of 0.7 Å. The white arrow symbolizes the solvent access to the tunnel. Water molecules present in the tunnel (PDB ID: 1Q16) are shown as red spheres. The average distances (based on the PDB ID: 1Q16, 1R27 and 1Y4Z) between the side-chain oxygens of Glu-581 and Asp-801 is 2.4 ± 0.1 Å; Glu-581 and Gln-234 3.6 ± 0.2 Å; and Glu-581 and Tyr-217 4.4 ± 0.3 Å. Residues are colored according to the *b*-factor value, where blue indicates structural rigidity and red indicates flexibility. The shape of the substrate tunnel in all three structures is nearly identical and therefore not shown for each structure separately. The images were created with PyMOL using PDB ID: 1Q16 (1.9Å resolution).

Interestingly, Glu-581 is surrounded by a set of conserved polar amino acids (Tyr-217, Gln-234 and Asp-801) and forms a hydrogen bond with Asp-801 (Fig. 2). To address the involvement of the hydrogen-bonding network of Glu-581 as well as the mechanistic importance of protonatable residues, determination of the kinetic parameters (K_m and k_{cat}) was performed at different pH values (Fig. 3 and S3). Remarkably, the K_m turned out to be highly sensitive to pH, increasing by one order of magnitude between pH 6 and 8.5 while k_{cat} was barely affected. This observation strongly suggests the presence of one or more protonatable residues (apparent pK_a about 7.7) of which the deprotonation impacts substrate affinity and or accessibility to the Mo active site. At higher pH values, the k_{cat} decreases indicating that deprotonation (apparent pK_a about 9) also leads to the loss of activity. Owing to the difference in these apparent pK_a values, this suggests that the two phenomena are not fully correlated and that the parameters that control substrate access and proton transfer are distinct.

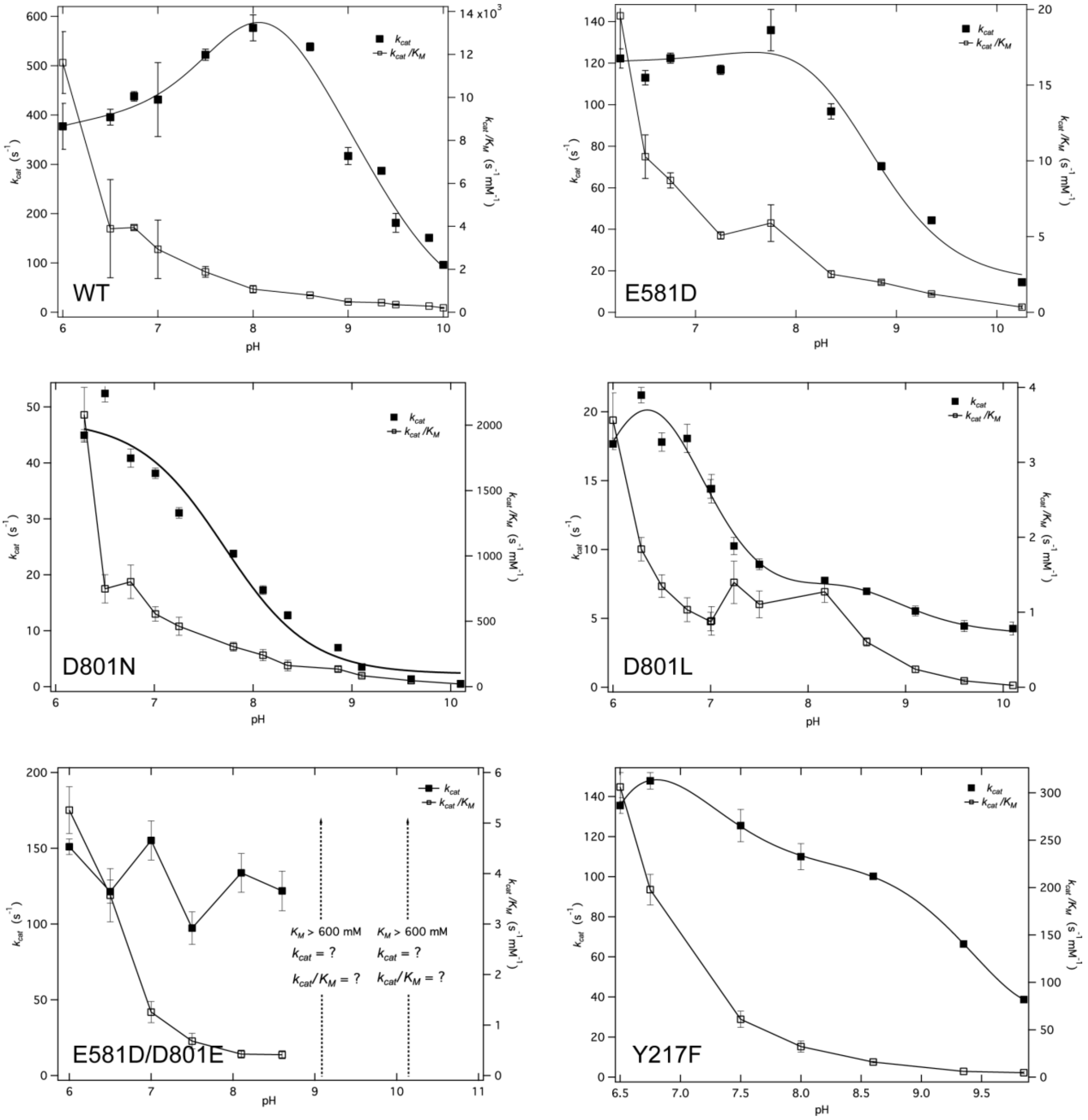

Figure 3. The pH dependence of the kinetic parameters k_{cat} and k_{cat}/K_{m}. For each pH value, the values and errors (SD) of the kinetic parameters are obtained from at least two *Michaelis-Menten* curves each with at least 10 points. The k_{cat} values were fitted according to Eq. 1 except for the E581D/D801E (see text). The pH profiles of the K_{m} are found in Figure S4.

Glu-581 is crucial for substrate binding and turnover. To get insight in the catalytic importance of the strictly-conserved Glu-581 in terms of hydrogen-bond formation and proton transfer capacity, E581D and E581Q variants were generated. Asp has a shorter side chain than Glu and the E581D variant is assumed to structurally influence the H-bond network while maintaining the proton transfer capability whereas the

E581Q variant is supposed to maintain the H-bond network while being unable to exchange protons. Such substitutions were shown to be very useful to probe the function of glutamate residues in other oxidoreductases such as hydrogenases (67) and ribonucleotide reductases (68). At first, the kinetic parameters of all enzyme variants were determined at pH 6.5, a value within the physiological pH range of the enzyme and giving a high k_{cat}/K_m (Table 1). E581D displays a k_{cat} for nitrate lower than that of the WT (about 3.5 fold) but of the same order of magnitude suggesting that catalysis is not drastically impacted. This is consistent with the similarity between the functional groups of Glu and Asp. In contrast, the K_m of E581D was significantly increased (by two orders of magnitude) indicating a crucial role of the precise localization of the carboxyl group of Glu-581 for substrate affinity and or accessibility. The kinetic parameters of E581D as a function of pH showed a similar pattern to those of the WT (Fig. 3 and S3). On the contrary, the k_{cat} of E581Q was decreased by three orders of magnitude while the K_m was identical to the WT within statistical error (Table 1). Due to the diminished activity, the kinetic parameters of this variant were only determined at pH 6.5. Interestingly, comparing the kinetic parameters of E581Q and E581D at pH 6.5 shows an inverted effect (Table 1). These data clearly reveal the importance of the acidic character of Glu-581 for turnover. At the same time, the role of Glu-581 in participating in the H-bonding network seems to be important for substrate affinity and or accessibility as indicated by the unaffected K_m of E581Q.

Table 1. Kinetic parameters k_{cat} and K_m of the NarGH variants assayed at pH 6.5 with either nitrate or chlorate.

	NO_3^- as substrate			**ClO_3^- as substrate**			**k_{cat}/K_m ratio**
	k_{cat} (s^{-1})	**Km (mM)**	**k_{cat}/K_m (s^{-1} mM^{-1})**	**k_{cat} (s^{-1})**	**K_m (mM)**	**k_{cat}/K_m (s^{-1} mM^{-1})**	**NO_3- vs. ClO_3-**
WT	396 ± 16	0.10 ± 0.06	3960 ± 2381	1031 ± 20	0.42 ± 0.03	2455 ± 182	1.6
E581D	113 ± 3	11 ± 2	12 ± 1.9	230 ± 9	11 ± 2	21 ± 3.9	0.6
E581Q	0.14 ± 0.004	0.15 ± 0.02	0.93 ± 0.13	0.16 ± 0.01	0.20 ± 0.04	0.8 ± 0.2	1.2
E581D/D801E	121 ± 8	34 ± 5	3.6 ± 0.57	99 ± 3	14 ± 2	7.1 ± 1	0.5
D801N	52 ± 2	0.03 ± 0.01	1733 ± 582	72 ± 3	0.09 ± 0.02	800 ± 181	2.2
D801L	18 ± 1	13 ±1	1.4 ± 0.13	14 ± 1	3.2 ± 0.5	4.4 ± 0.75	0.3
Y217F	136 ± 1	0.44 ± 0.03	309 ± 21	84 ± 3	0.36 ± 0.06	233 ± 40	1.3
Y217F/D801L	1.1 ± 0.03	14 ± 1	0.079 ± 0.01	2.0 ± 0.1	12 ± 2	0.17 ± 0.03	0.5

Ratio of the specificity constants of the variants compared to the WT with nitrate or chlorate as substrates. The values and error estimations (SD) are obtained from at least two *Michaelis-Menten* curves with at least 12 points each.

Acid-base properties and H-bonding ability of Glu-581 are strongly modulated by its polar environment. According to the available crystal structures, the closest residue able to form strong H-bonds with Glu-581 is Asp-801 (Fig. 2). Evaluation of the role of such H-bonds and of the acid-base properties of Asp-801 was performed using the D801N and D801L variants. D801N is a neutralization polar variant lacking the acidic property but still able to maintain H-bonds (substitution analogous to E581Q), while the hydrophobic D801L variant prevents both the proton exchange and the formation of H-bonds. The kinetic parameters of the D801N variant show a lower K_m by nearly an order of magnitude than that of the WT and E581Q variant. In contrast, the D801L variant displays a major increase in K_m (Table 1). With comparable k_{cat} values for both D801 variants, one can assume that the H-bond forming ability of Asp-801 plays a major role in substrate affinity. Moreover, D801N displays a high catalytic activity of nearly 400-fold higher than that of E581Q (Table 1) showing that the acidic character of Asp-801 is not as essential as that of Glu-581 but its H-bonding capability is. Interestingly, the pH-dependence profiles of k_{cat} and K_{m} of the Asp-801 variants (Fig. 3 and S3) show a global shift to a more acidic pH when compared to the WT. Notably, by comparison with WT and E581D (pK_a about 9), the k_{cat} acidic profile is shifted by one pH unit for D801N (pK_a about 7.8) and reaches about two pH units for D801L. This suggests that the Asp-801 substitutions affect the same protonatable group involved in catalytic proton exchange. Considering that this protonatable group corresponds to the carboxylic chain of Glu-581, these results suggest that the H-bonding between Asp-801 and Glu-581 induces a strong acid-base cooperativity between the carboxylic/carboxylate pairs of these residues. Acid-base cooperativity refers to the fact that the pK_a of an acid can depend on the ionization state of the acid-base pairs in its vicinity. This is notably the case when the acid-base pairs are linked by H-bonds where pK_a shifts of several units have been observed (69). In NarGH such cooperativity could increase the pK_a of Glu-581 and facilitates protonation/deprotonation during turnover at physiological pH.

Furthermore, H-bonding potential of these residues appears critical to control substrate access as deduced from the increase by two orders of magnitude of K_{m} for the D801L variant with poor pH dependency except at very high pH, while k_{cat} decreases only 20-fold in comparison to WT (Fig. S3 and S4). This is also supported by the similar K_{m} values observed for the WT, E581Q and D801N variants, while the strong increase of K_{m} for E581D suggests either a disruption of the E581-D801 H-bond or a significant change of the relative arrangement of these two acidic residues. Hence, reversing the position of the two residues was expected to restore this H-bond and lowers K_{m}. Surprisingly, while the E581D/D801E variant exhibits an activity similar to that of E581D and WT, which is consistent with the presence of an acidic residue at position 581, its K_{m} value increased by more than two orders of magnitude with respect to WT (Table 1). In addition, the pH-dependence of the E581D/D801E K_{m} shows at least one order of magnitude increase between pH 6 and 8.5, similarly to the WT and E581D (Fig. S3). Altogether, these observations indicate that the existence of a H-bond between Glu-581 and Asp-801 is important for substrate affinity but is likely not the sole determining factor. The data also indicate that the precise spatial positioning of the acidic groups of Glu-581 and Asp-801 is also required for efficient substrate binding suggesting the involvement of other polar residues in a rather intricate and dynamic H-bonding network.

To gain more insight in the effect of the polar environment of Glu-581 on the workings of the enzyme, we identified Tyr-217 as an interesting target based on its short distance from Glu-581 (Fig. 2) and its localization in the same loop as the Mo coordinating ligand (Asp-222). Two hydrophobic Y217F and Y217F/D801L variants were generated and subjected to kinetic measurements. The data show that the k_{cat} value of Y217F is reduced by a factor of about 3 by comparison with WT while K_{m} has increased by a factor of about 4 (Table 1). Importantly, the maximum activity of Y217F has shifted to the more acidic pH region with respect to the WT similar to what was observed in the Asp-801 variants, supposedly due to the perturbation of the H-bonding network (Fig. 3 and S3). In contrast, the Y217F/D801L double variant showed both a major decrease of k_{cat} and an increase in K_{m} (Table 1). The behavior of the Y217F and Y217F/D801L variants suggests that the hydroxyl group of Tyr-217 helps to fine-tune the pK_a values of acidic residues involved in the catalytic proton exchange, and that the effects of the hydrophobic substitutions on the kinetic parameters are additive.

H-bond network involving Glu-581 is responsible for substrate selectivity. Consistent with the peculiar positioning of Glu-581 at the bottleneck of the substrate channel, kinetic studies performed with nitrate as substrate unequivocally show that its acidic character and H-bonding ability with Asp-801 are essential for both turnover and substrate affinity (Fig. 3 and Table 1). To analyze the influence of Glu-581 and its polar environment in substrate selectivity, we have extended our kinetic measurements to include chlorate (ClO_3^-), an alternative substrate for Nar. Chlorate has a slightly larger ionic radius than nitrate and, in contrast to the latter, it has a dipole moment due to its pyramidal structure. NarGH has slightly higher specificity constant given by the k_{cat}/K_m ratio towards nitrate together with a lower K_m for nitrate (Table 1 and Fig. S4) (16). Overall, the k_{cat} variations with chlorate with respect to WT follow the same trends to that observed with nitrate (Table 1 and Fig. S4), the strongest decrease being observed for E581Q, D801L and Y217F/D801L. This shows that the same factors are responsible for catalysis with the two anions, namely the acid-base properties of Glu-581. Changes in k_{cat} and K_m result in the modification of the substrate selectivity of the enzyme that can be assessed by comparing the specificity constant (70). With the exception of D801N, in most of the studied variants the ratios between the k_{cat}/K_m of nitrate versus chlorate approaches one (E581Q, Y217F) or is even lower (E581D, E581D/D801E, D801L, Y217F/D801L) which indicates that these variants have lost their discriminatory capacity between nitrate and chlorate (Table 1). Overall, the data show that all substitutions suggested to compromise the H-bonding ability of Glu-581 with its polar environment, change the substrate specificity leading to a higher specificity constant towards the polar substrate, chlorate (Table 1).

To get more insight in the contribution and interplay of the polar residues in the H-binding network, differences in transition-state energies, $\Delta\Delta G_{ES},^{\ddagger}$ have been calculated from the k_{cat}/K_m values (Eq. 2). Briefly, with this approach one can assess the thermodynamic contributions of structural components that are involved in the stabilization of the transition state of the substrate-enzyme complex, $ES^{\ddagger}$ (53). The difference in transition-state energy was calculated for each Nar variant relative to the WT either with nitrate or with chlorate as well as for a given variant with chlorate relative to nitrate (Table S3). The negative $\Delta\Delta G_{ES}^{\ddagger}$ values of the variants relative to the WT (regardless of the substrate) show that all substitutions increase the transition-state energy, leading to less efficient catalysis. The lowest perturbation of the $\Delta\Delta G_{ES}^{\ddagger}$ value is found for D801N in which the H-bond with Glu-581 is likely maintained with the same structural organization. In contrast, the most negative values are obtained in variants where the H-bonding capacity of Glu-581 and Asp-801 is potentially disrupted (D801L, Y217F/D801L, E581D) and in this case the $\Delta\Delta G_{ES}^{\ddagger}$ value is close to the energy of an H-bond (4-5 kcal/mol). It is notable that the variant vs. WT $\Delta\Delta G_{ES}^{\ddagger}$ of Y217F/D801L corresponds well to the sum of the values obtained for the Y217F and D801L single variants revealing independent effects of the substitutions on catalysis. This suggests that the H-bonds of Glu581 with Asp-801 and Tyr-217 act as independent factors on substrate selectivity and catalysis by controlling the acid-base properties of Glu-581 and ensuring a good positioning of its side-chain.

Influence of the hydrogen bond network involving Glu-581 on the molybdenum cofactor spectroscopic and redox properties. Wild type nitrate reductase has two well characterized Mo(V) species whose relative proportions depend on pH, namely a high pH species with $g_{1,2,3}$ = 1.987, 1.980, 1.962, and a low pH species with $g_{1,2,3}$ = 2.001, 1.985, 1.964. The latter displays a resolved proton hyperfine splitting characterized by an anisotropic hyperfine coupling tensor with principal values $A_{1,2,3}(^1H)$ = (1.17, 0.88, 0.99) mT. The *g*-tensor analyses indicate a similar first coordination sphere of the Mo(V) ion in both species (5, 71). It has been shown that their interconversion does not correspond to a simple acid-base equilibrium but is rather due to distant modifications of the H-bond network around Mo cofactor (20, 21). To analyze the role played by Glu-581 and its polar environment on the structural and redox properties of the Mo active site and other metal centers, we used EPR spectroscopy. To this end, the E581D, E581Q and Y217F/D801L variants were selected based on expected alteration of the H-bonding to Glu-581 induced by each of the substitution. The NarGH variants enriched in the nuclear spin I = 0 ^{98}Mo isotope were prepared at pH 7.5, titrated and studied by EPR spectroscopy, together with the WT for comparison. The typical Mo(V) EPR signatures detected in these samples are shown in Figure 4 while their redox behavior is depicted in Figure S5. The WT exhibits the two well characterized high pH and low pH Mo(V) species, both representing a maximal total amount of about 0.4 spin/NarGH (Fig. 4A-B) which is typical of NarGH preparations (17, 19-21). More generally, such sub-stoichiometric amounts of Mo(V) EPR species are commonly observed in the enzymes of the Mo-*bis*PGD family and are even lower in enzymes such as Nap, where they account for less than 0.2 spin/molecule (72-74). In contrast, only the high pH Mo(V) species is detected in the E581Q variant with a maximal amount of 0.25 spin/NarGH (Fig. 4C). This holds also true when the sample is prepared at pH 6.4 (Fig. S6C), a value at which the low pH species is predominant in the WT (Fig. S6A-B). The E581D substitution strongly affects the intensity and the shape of the detected Mo(V) EPR signal (Fig. 4D). The latter could be simulated by considering three different Mo(V) species, namely the high and low pH species, and an additional species with $g_{1,2,3}$ = 2.0263, 1.9896, 1.9739 (Fig. 4E and Table S2). The latter possesses a remarkably high g_1 value and is not observed in the EPR spectra of the WT or of the E581Q variant. It is referred to as “high g_1” species in the remainder of the text. The Mo(V) EPR signal maximally accounts for about 0.08 spin/NarGH in the E581D variant, where the maximal contribution of the high g_1 species represents about 30% of the total Mo(V) content. Strikingly, only the high g_1 Mo(V) species amounting to about 0.02 spin/NarGH was observed in the Y217F/D801L variant while no high pH or low pH Mo(V) species were detected (Fig. 4F). Interestingly, the g-values of this high g_1 Mo(V) species are correlated to those of the high and low pH species observed in Nar from different organisms (Fig. S7). Such correlation is indicative of a similar first coordination sphere of the Mo ion in these three species and, in this case, corresponds to a coordination of the MoS_4O_2-type (5, 63, 64). Overall, these observations suggest that perturbations of the H-bond network around the Mo cofactor or at remote positions such as near Glu-581 induce conformational fluctuations responsible for the different Mo(V) EPR species observed. The results of Glu-581 substitutions indicate that the acidic character rather than the H-bonding capacity of Glu-581 is necessary for the generation of both the low and high pH Mo(V) species in NarGH which show no significant variations of their g-values between variants. Moreover, whereas the redox potential of the one electron Mo(V)/Mo(IV) transition (E_2) has been barely modified by Glu-581 substitutions, that of the Mo(VI)/Mo(V) transition (i.e. E_1) is more significantly affected, with about 130 mV increase for the high pH Mo(V) intermediate and about 70 mV decrease of the low pH one (Table 2 and Fig. S5). In addition, the redox properties of the high g_1 Mo(V) species in E581D and Y217F/D801L variants are very similar (Table 2).

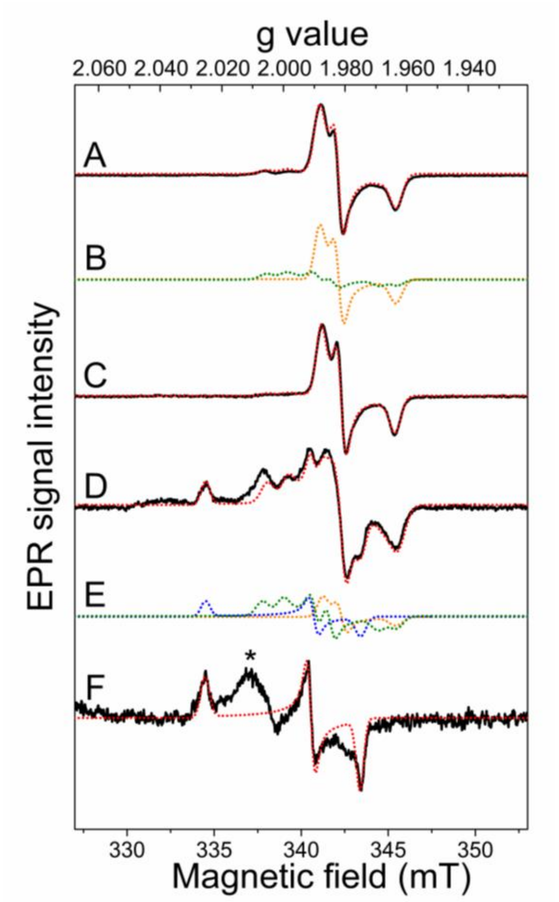

Figure 4. Mo(V) EPR spectra of ^{98}Mo-enriched NarGH enzymes poised at different potentials at pH 7.5: (A) WT, +161 mV; (C) E581Q, +197 mV; (D) E581D, +124 mV; (F) Y217F/D801L, +200 mV. Experimental spectra are in black and simulations are superimposed as red dotted lines. Simulations were performed by adding the spectral contribution of high-pH (orange), low-pH (green) and high-g_1 (blue) Mo(V) species with parameters and proportions given in Table S2. These spectral contributions are shown in (B) for WT and in (E) for E581D. Experimental conditions: temperature, 50 K, microwave frequency, 9.4803 GHz (A), 9.4789 GHz (B), 9.4802 GHz (C), 9.4799 GHz (D); microwave power, 0.25 mW (A, C) or 4 mW (D, F); field modulation amplitude, 0.2 mT (A, C) or 0.4 mT (D, F); number of scans, 4 (A, C), 1 (D), or 10 (F). The asterisk on spectrum F shows the contribution of a contaminant radical species.

Table 2. Molybdenum redox properties in wild type NarGH and in the E581Q, E581D and Y217F/D801L variants, at pH 7.5.

		$E_2°'_{7.5}$ (Mo^{V}/Mo^{IV}) (mV)	$E_1°'_{7.5}$ (Mo^{VI}/Mo^{V}) (mV)	E_m (mV)
WT	High pH	35 ± 10	230 ± 10	135
	Low pH	20 ± 10	> 440	> 245
E581Q	High pH	70 ± 20	360 ± 25	215
E581D	High pH	10 ± 10	365 ± 15	190
	Low pH	30 ± 10	370 ± 40	200
	High g_1	25 ± 20	> 450	> 250
Y217F/D801L	High g_1	75 ± 20	> 470	> 265

Overall, these results show that in all variants studied, the intermediate Mo(V) species have the same first coordination sphere and retain a broad stability domain of several hundred mV around circa +200 mV, suggesting that the chemistry at the Mo site is not altered. These species likely differ in the conformation of the Mo surrounding and, in agreement with our previous data (19), our results indicate that the high pH and high g_1 Mo(V) species alone do not enable enzymatic activity. On the other hand, the results support the previous hypothesis that the low pH Mo(V) intermediate is linked to enzyme catalysis (75) and that interconversion of high to low pH Mo(V) species is possibly involved in enzyme turnover (19-21).

Beside the EPR signal of the Mo cofactor, the detectable EPR signatures of the NarH S = ½ FeS clusters were similar in the three variants and in the WT. In addition, the two characteristic low-field components at g = 5.0 and 5.6 of the S = 3/2 FS0 cluster with E_0’ ~ -55 mV in the WT enzyme (12, 18, 47) (Fig. S8A) were detected in both Glu-581 variants (Fig. S8B and C). In contrast, these were not resolved in the

Y217F/D801L variant (Fig. S8D and E), even at much lower (about -430 mV) redox potentials, revealing a significant perturbation of the FS0 structure and/or redox properties upon disruption of the H-bond network around Glu-581. In conclusion, the EPR data point to an important structural role of the H-bond network involving Glu-581, Tyr-217 and Asp-801 for maintaining the structural conformation and surroundings of the molybdenum cofactor.

Glu-581 motions reconfigure the local hydrogen bond network. The X-ray structure of Nar from *E. coli* indicates that Glu-581 is located at the middle of an L-shaped loop (His-576 to Pro-585) that contacts the Mo atom at the level of Gly-579 which is only 3,65 Å apart, hereinafter referred to as Glu-loop (Fig. 5A). As evidenced by three distinct MD simulations of the wild type NarGH apoprotein (see Materials and Methods), the Glu-loop and Glu-581 exhibit important conformational changes (Fig. 5B).

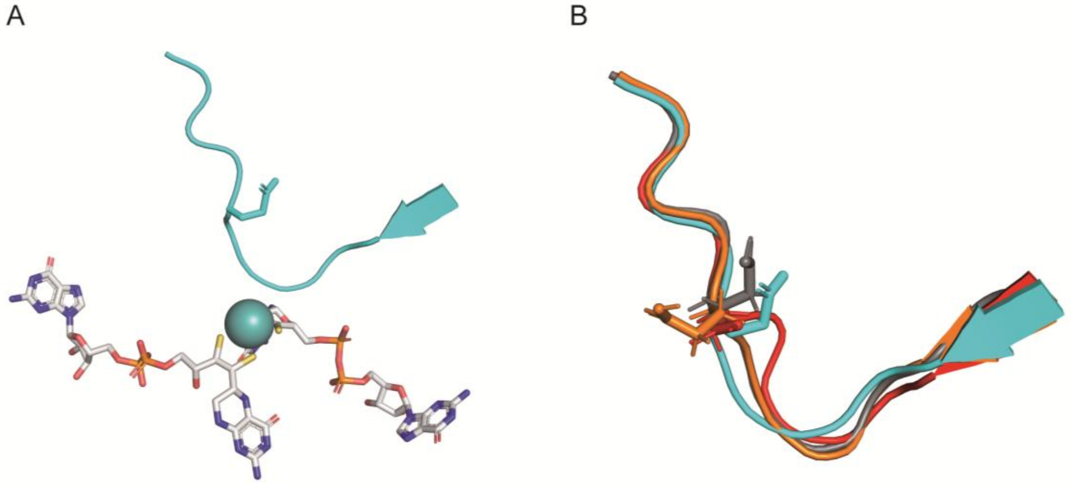

Figure 5: Conformation of the Glu-loop supporting the Glu-581 residue (from 575 to 586) (A) in the NarG holo structure (PDB ID:1Q16) and (B) in the three simulations. In B, the three loop structures averaged over the simulation time are shown in cartoon representation along with the Glu-581 residue in bond representation. Simulation 1 (grey) retains the loop structure found in the apoprotein crystal structure (cyan). In Simulation 2 (red), a structural refolding involves the Glu-loop. In Simulation 3 (orange), the structure of the loop is retained but a flip of the Glu-581 side-chain occurs.

Furthermore, the analysis of potential H-bonds involving the Glu-581 side chain (Table 3) indicates that the local dynamics of the Glu-loop strongly influences the H-bond network. The structure of the Glu-loop from simulation 1 is very similar to what is observed in the crystal structure (PDB ID: 1Q16) showing one H-bond between Glu-581 and Asp-801. Conversely, simulation 2 displays important local refolding (Fig. 5B) with two major sterical consequences. First, the distance between Glu-581 and Asp-801 is increased leading to the breakage of the Glu-Asp H-bond and the formation of a transient H-bond between Glu-581 and Gln-234 (Table 3). Second, the local refolding displaces the loop slightly away from the Mo active site. Interestingly, in simulation 3, the backbone remains at the same position as for simulation 1 but the Glu-581 side-chain reorients towards Gln-234 instead of Asp-801 resulting in a stable H-bond. Importantly, none of the simulations show the formation of a H-bond between Glu-581 and Tyr-217. These results provide computational evidence for the dynamics of the Glu-loop buried in NarG as suggested by the high *b* factor observed in the X-ray structure and correlate these dynamics to changes in the H-bonding network in the vicinity of the active site. Interestingly, Table 3 shows that Glu-581, Asp-801 and Gln-234 participate to numerous H-bonds with water molecules. These residues are on average involved in one to four H-bonds (H-bond occurrence ranging from 100 to nearly 500%). The degree of hydration of these residues is highly modulated by the motion of the Glu-581 side chain. While simulation 1 shows that Asp-801 forms a H-bond with a single water molecule, simulations 2 and 3 show increased hydration of Asp-801 upon disruption of the H-bond with Glu-581. If the motions recorded in MD simulations are related to functional roles, their alterations, for example by substitutions, could reconfigure the local H-bond network. These results support the involvement of Glu-581 and Asp-801 in the H-bonding network near the active site as was suggested by mutational and kinetic experiments in this work. In addition, the MD simulations suggest an important role for water molecules in mediating the effect of amino acid substitutions at positions distant from the Mo active site.

Table 3: Hydrogen-bond occurrence in MD simulations and in the NarGH X-ray structure

H-Bond	Simulation 1	Simulation 2	Simulation 3	H-bond in PDB ID:1Q16
E581-D801	93.2%	0.2%	2.5%	1
E581-Q234	3.4%	18.2%	94.2%	0
E581-Y217	0%	0%	0%	0
Q234-water	279%	259%	169%	1
E581-water	215%	307%	291%	1
D801-water	104%	323%	472%	3
Y217-water	9.5%	4.8%	0.3%	0

H-bond occurrence is defined when the distance between donor (D) and acceptor (A) is < 3.5 Å and the angle formed by atoms H, D and A is < 30 °

Glu-loop motions connect the bulk cavity to the active site via a "water wire". To further evaluate the relationship between protein motions and hydration, the average water density was computed for the three MD simulations (Fig. S9) and the diffusion of individual water molecules followed during the course of the simulations (Fig. 6). In simulation 1, water molecules can be distinguished into three spatial groups (Fig. 6A and movie S1): the first one is located in the substrate tunnel (cyan), the second one is positioned in a site located between Glu-581 and Asp-801 (green) and a third one is located in the Mo active site cavity (blue). Importantly, the water molecules do not move between the different areas, consistent with the water density data (Fig. S9) which show that the different cavities are not interconnected. Upon local refolding of the Glu-loop as seen in simulation 2, water molecules (cyan) can diffuse through the three cavities (Fig. 6B and movie S2) testifying to the opening of a channel. First it explores the active site area, then it crosses a newly open intermediate tunnel to end its diffusion to the bulk through the substrate tunnel. Another water molecule (dark blue) whose trajectory overlaps with the former is able to diffuse to a place where the Mo should be and find a coordination site nearby. Such behavior could be made possible through the opening of an intermediate tunnel originating from the Glu-loop displacement described in Figure 5. The existence of this tunnel along the trajectory is confirmed by water density calculations (Fig. S9). When the Mo-*bis*PGD cofactor is superimposed to this water trajectory, no overlap is observed indicating that the opening of this channel is compatible with the structure of the holoprotein. Given the small water volume available in the active site pocket of the holoprotein, diffusion of water or substrates towards the Mo through this channel can therefore be very efficient. Since water can go from the bulk to the Mo position in simulation 2, this situation can be seen as an open state.

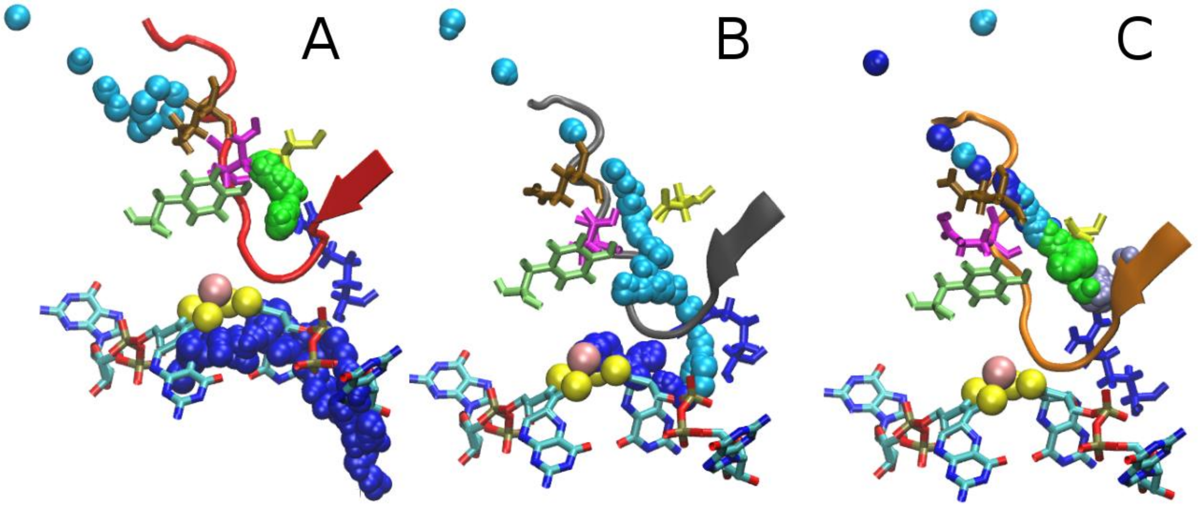

Figure 6: The Glu loop motions can open a water tunnel from the bulk to the active site. On each panel, the Glu-loop is represented as in Figure 5. To depict the position of the active site, the Mo-*bis*PGD cofactor (represented as mixed bonds and van der Waals spheres) has been fitted on the protein (see Materials and Methods). The motion of various water molecules (depicted by distinct color codes) is represented over multiple frames for simulation 1 (A), simulation 2 (B) and simulation 3 (C). On each panel residues that delineate the border of a potential channel are represented as bonds, including Gln-234 (brown), Glu-581 (purple), Asp-801 (yellow) Tyr-157 (green) and Arg-260 (blue).

In simulation 3, where only the E581 side chain has flipped, two water molecules initially present in the intermediate tunnel can reach the substrate tunnel and the bulk of solvent (cyan and dark blue) (Fig. 6C and movie S3). In the timescale of this simulation (extended to 200 ns), two other water molecules more deeply embedded in the tunnel structure remain trapped close to their original place (gray and green). These MD simulations suggest that the motion of the Glu-581 side chain as for simulation 3 allows to connect the intermediate tunnel to the substrate entry tunnel but the Glu-loop movement seen in simulation 2 is obligatory to achieve a complete connection and the transport of water molecules between the bulk and the Mo active site. Considering that the same channel could be involved in substrate transport from the bulk to the active site, it is not surprising that our designed substitutions have strong effect on the substrate affinity. Furthermore, in the intermediate tunnel of the open form (simulation 2), the water organizes into a single row of four successive molecules forming hydrogen-bonded chains of water molecules (Fig. 7). Such a water wire connects the acidic side chains of Glu-581 and Asp-801 to the bottom of the main entry cavity and next to the His-576 residue (which is located at the top of the active site cavity) thus promoting the possibility of proton transfer through a Grotthuss hopping mechanism (76, 77). The residues that could participate in proton transfer via the coordination of water molecules are given in Figure S10. Interestingly, almost all the residues proposed are conserved in the two structurally well-characterized Mo/W-*bis*PGD enzymes (nitrate reductase and perchlorate reductase), further supporting the existence of the channel (Table S4).

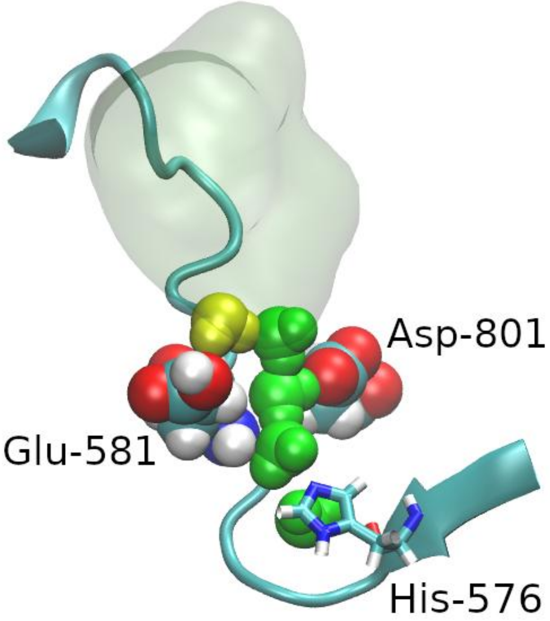

Figure 7: A water wire in the path of a candidate channel. In the open state conformation (final structure in simulation 2) four successive water positions (green) connect the bottom of the main entrance cavity (represented as a yellow water molecule and a transparent surface) to the acidic E581 and D801 residues until the H576 residue.

Discussion

The yet uncovered range of reactivities of Mo/W-*bis*PGD enzyme superfamily members sharply contrasts with the limited chemical diversity of their Mo/W active sites. This prompted us to investigate the importance of remote positions in fine-tuning the reactivity of the active site. In all members, the Mo/W active sites are buried inside the protein and connected to the bulk solvent through a funnel-like entrance, which likely acts as the exchange pathway for the substrates, products and solvent molecules during the catalytic cycle. Importantly, for many of them including Nar (PDB ID: 1Q16), Pcr (PDB ID: 4YDD) or Ebd (PDB ID: 2IVF), the funnel-like entrance terminates at a location distant from the active site raising the question on how substrate or solvent access is made possible. Enzymes often possess the structural elements for controlling the transport of substances through tunnels by means of a gate which can switch between open and close states through conformational changes and by this way controls the passage of molecules into and out of the protein (78). Here, we provide strong evidence that a set of conserved polar residues remote from the active site controls the transport of substrates and Mo reactivity.

Determination of kinetic parameters at different pH values revealed that deprotonation events are associated with a strong decrease in substrate affinity or accessibility but also in catalytic turnover suggesting the involvement of one or more protonatable residues. Our rationale was that if access to the active site is distantly controlled by a gate involving a series of polar residues, protein substitution can modulate the solvation of the active site but also ligands exchange and thus enzyme activity and selectivity. Two interconnected but distinctive roles have been associated with these residues, proton transfer and substrate affinity or accessibility.

The conserved Glu-581 located at the bottleneck of the tunnel is suggested here to play the most important role in proton transfer. While being surrounded by several conserved polar residues and exhibiting a strong acid-base cooperativity with Asp-801, the acidic character of Glu-581 is essential for turnover but its ability to form H-bonds appears to be a criterion for substrate affinity. The molecular simulations presented here suggest that H-bonding ability of Glu-581 with its polar environment and in particular with Asp-801 controls the hydration inside the protein core. We observed that the motion of Glu-581 (and Glu-loop) results in the formation of a proton-conducting water channel that connects the active site to the bulk solvent. Those observations are consistent with the fact that perturbations of the H-bond network at remote positions such as near Glu-581 influence the generation of low and high pH Mo(V) species as well as induce conformational fluctuations of the Mo cofactor resulting in novel Mo(V) species with similar first coordination sphere but different catalytic activities. This is in complete agreement with the demonstration that the conversion between the low pH and the high pH Mo(V) species is not related by a simple acid-base equilibrium (20). The presence of the low pH Mo(V) species being correlated with a high k_{cat} value supports the involvement of this species in enzyme turnover as suggested before (19). Substitutions of Glu-581 thus influence the Mo redox properties as those of residues coordinating the pyranopterin moieties in Nar (8) or in arsenite oxidase (9). Our study underlines the importance of the H-bond network of the substrate channel in fine-tuning the reactivity of the Mo active site.

Experiments also support a mechanistic role of Glu-581 in substrate affinity.

Disturbance in the H-bonding between Glu-581 and Asp-801 upon substitution, by diminishing the strong acid-base cooperativity, likely reduces the apparent pK_a of Glu-581 whose role in proton exchange is essential during turnover. Spatial positioning of the corresponding functional groups is also key for high substrate affinity and supports the Glu-581 motion observed by molecular dynamics simulations. Given that polar charge-neutral E581Q and D801N variants display high substrate affinity, both residues are likely protonated upon substrate binding. Interestingly, the K_m pH-profile of D801N shows weak pH-dependence consistent with the non-deprotonatable asparagine and thus suggesting that the increase in K_m for the WT is mainly due to the deprotonation of Asp-801. Based on this analysis, it is very plausible to assign a pK_a of about 7.7 to Asp-801. Assuming that turnover is directly dependent on the ability of Glu-581 to exchange protons, the decrease in activity of WT Nar at higher pH values may be prescribed to the deprotonation of Glu-581 (pK_a about 9). This is supported by the k_{cat} pH-profile of D801N, which displays a shift to lower pH pointing to a decrease in the pK_a. Strong acid-base cooperativity as well as charge-dipole interactions can highly modulate amino acid properties, such as the pK_a, to serve protein stability or catalysis as reviewed in (69) and explain the high pK_a values we report here. Deprotonation of Glu-581 may also be favored by a modification of its immediate environment during side-chain motions. Furthermore, substrate affinity and selectivity appear to relate to the H-bonding potential of a series of conserved polar residues located between the bottleneck of the funnel-like entrance and the Mo active site. All substitutions compromising the H-bonding ability of Glu-581 with its polar environment impede the enzyme specificity towards nitrate and chlorate albeit a similar trend is observed for both substrates in the variants. Our data demonstrate that Glu-581 has multiple functions as it serves in proton transfer, substrate selectivity and, suggested by molecular simulations, as a gate that opens and closes the pathway to the Mo active site. Gates provide enzymes with advanced capabilities for selecting the molecules allowed to enter the active site but also control their rate of transport as illustrated in NiFe hydrogenases (38, 79) and can also facilitate proton transport through water-gated transitions such as in the respiratory complex I (80).

Given the strong structural similarities between Nar and perchlorate reductase or ethylbenzene dehydrogenase (15, 16) as well as their grouping in a distinct clade in the phylogenetic tree of Mo/W-*bis*PGD enzymes (1, 81), we not only considered the conservation of the above-mentioned residues but also looked at the conservation of putative gating mechanisms in other members of the enzyme superfamily. As stated before, the funnel-like entrance dimensions are similar in *Azospira suillum* Pcr and *Escherichia coli* Nar as well as the distance between the bottleneck and the Mo atom (16). Furthermore, most of the residues involved in the water path coordination are conserved or can maintain the same type of interactions (Fig. S11 and Table S4). The gating residue Glu-581 in Nar is replaced by the aromatic Trp-461 in PcrA which occludes the access to the active site. Interestingly, the W461E variant shows a defect in both chlorate and nitrate affinity or accessibility as evidenced by the large increase in K_m (3 to 700-fold, respectively) while k_{cat} is little affected (16). As illustrated in Figure S11, it is likely that the W461E substitution is not sufficient to allow optimal nitrate access, and thus a change in selectivity, due to the involvement of a dedicated polar amino acid network as revealed in our study of Nar. In the crystal structure of the reduced enzyme, alternative conformations have been found for Phe-164 (equivalent to Phe-216 in *Ec*Nar) resulting in tunnel closing or opening (16). In the crystal structure of *Aromatoleum aromaticum* Ebd, the substrate tunnel is significantly deeper and clearly features a bottleneck at a distance about 15 Å from the Mo atom made up of hydrophobic amino acids Trp-200, Phe-956, Val-489 and the charged Asp-485 (15). Thereof, access to the active site for the bulky substrate ethylbenzene requires local conformational changes.

Those observations prompted us to verify the situation in the distantly-related periplasmic nitrate reductases (Nap) which display a different first coordination sphere of the Mo/W atom while performing the same reaction. Their funnel-like entrances share some similarities such as being occluded at approximately the same distance from the active site, about 10 Å (Fig. S11). The residue that constricts the tunnel is a conserved arginine (Arg-418, *E. coli* Nap numbering) involved in a salt bridge with a conserved aspartate (Asp-194) in all X-ray structures available for Nap (29, 34, 82, 83). Site-directed mutagenesis of the conserved Arg has been performed in several Naps (84, 85) or even in the phylogenetically related assimilatory nitrate reductases (86, 87). The R421E variant in *Ralstonia eutropha* Nap shows a complete loss of activity (84), whereas the R392A substitution in *Rhodobacter sphaeroides* Nap increases K_m^{nitrate} by more than one order of magnitude without affecting k_{cat}, testifying to a problem of affinity or accessibility for the substrate (85). The absence of Mo(V) signals in this variant (85) is consistent with the long-range repercussions observed in Nar during this study. A similar observation is made with the assimilatory nitrate reductase from *Synechococcus* sp. PCC 7942 (87) or *Cyanothece* sp. PCC 8801 (86) where substitution of the conserved Arg results in a dramatic decrease of the activity and modification of the redox properties of the Mo center. As such, the overall mechanism described here for Nar could be conserved in other members of this enzyme superfamily and suggests the participation of remote residues in tuning enzyme reactivity.

However, deeper understanding of Mo/W active sites reactivity requires more structural information, for example at different redox states, which is only available for a few members of the Mo/W-*bis*PGD superfamily, namely *A. suillum* perchlorate reductase (16) and *Desulfovibrio vulgaris* Hildenborough formate dehydrogenase (DvFdh) (37). In both enzymes, redox-induced local conformational changes were sufficient to strongly influence accessibility to the Mo/W active site with the remarkable absence of modification of the hydrogen-bond network surrounding the pterin moieties. While alternative conformations of a Phe residue controls tunnel opening in Pcr, a conserved His residue in DvFdh switches between two tunnels that are considered to be mutually exclusive. Interestingly, protein motion has long been observed in NADH:ubiquinone oxidoreductase and suggested to contribute to long range proton translocation. Indeed, molecular simulations revealed that those local conformational changes are responsible for cooperative hydration changes which result in the formation of proton-conducting channels connecting the protein interior and surface, even responding to the presence and redox state of the substrate quinone (80, 88-90).

In conclusion, our work underscores the significance of a remote region of the Mo/W-*bis*PGD catalytic protein core, the bottleneck region in modulating reactivity and fine-tuning Mo active site properties. Most importantly, this work paves the way to future studies aiming at defining molecular determinants for Mo/W-*bis*PGD enzyme reactivity and possibly oxygen resistance in oxygen-sensitive enzymes.

Supporting information

Figure S1: Root mean square deviation calculations of the NarGH subunits relative to that of the minimized experimental structure.

Figure S2: Conservation degree of residues identified at the bottleneck of the funnel-like entrance in *Escherichia coli* nitrate reductase A.

Figure S3. The pH dependence of the kinetic parameters k_{cat} and K_M.

Figure S4. Kinetic properties of wild-type and NarG variants assayed at pH 6.5 with either nitrate or chlorate as substrate.

Figure S5: EPR-monitored redox titrations of Mo(V) species in NarGH at pH 7.5.

Figure S6: Experimental and simulated Mo(V) EPR spectra of ^{98}Mo-enriched NarGH WT (A), E581Q (C), E581D (D).

Figure S7: Plot of the g-values of Mo(V) species against g-anisotropy in Nar or in Aio from different organisms.

Figure S8: EPR spectra of FS0 in wild type NarGH (A), E581Q (B), E581D (C) and Y217F-D801L (D, E) variants.

Figure S9: Water densities calculations averaged over the trajectories during the closed and open state simulations.

Figure S10: Water coordination in the path of a candidate selectivity channel.

Figure S11: Comparative analysis of amino acid residues involved in the bottleneck of the funnel-like entrance in (A) periplasmic nitrate reductase, (B) Ethylbenzene dehydrogenase, in the oxidized or reduced form of perchlorate reductase (C).

Movie S1: Motion of selected water molecules in the closed channel (simulation 1).

Movie S2: Motion of selected water molecules in the open channel (simulation 2).

Movie S3: Motion of selected water molecules in the semi-open channel (simulation 3).

Table S1: Oligonucleotides list

Table S2: Simulation parameters of the Mo(V) species detected in the wild type and NarGH variant enzymes at pH=7.5.

Table S3. The transition-state energy differences ($\Delta\Delta G^{\ddagger}$) of the variants compared to the WT with nitrate as substrate (vs. WT with NO_3^-) or chlorate (vs. WT with ClO_3^-) as substrates and those for the same variant but with chlorate compared to nitrate (ClO_3^- vs NO_3^-).

Table S4: Residues displaying polar contacts with water molecules in *Escherichia coli* Nar showing their degree of conservation in Nar, Nxr, Pcr and Ebd.

Table S5: Molybdenum content analysis obtained by ICP-MS. The measurement uncertainty for the detection of Mo is estimated to 5%.

Acknowledgments

The authors are grateful to the EPR facilities available at the national EPR network RENARD (IR CNRS 3443) and the Aix-Marseille University EPR center. This work was funded by the CNRS, Aix-Marseille University, the A*Midex foundation of Aix-Marseille University (project MicrobioE, grant number ANR-11-IDEX-0001-02) and the Agence Nationale de la Recherche (MOLYERE project, grant number 16-CE29-0010-01). Several authors are part of the FrenchBIC and of the GDR Solar Fuels. We deeply acknowledge the support of Dr. René Toci at the initial stage of this project and Dr. Athel Cornish-Bowden and M.L. Cárdenas for discussion and careful reading of the manuscript. This work was also supported by the GENCI-CINES for the use of high-performance computing resources (grant number A0010707044).

Authors' contribution

SA has performed mutagenesis, protein preparation, kinetics experiments and analysis of kinetics data. FS has performed mutagenesis and protein preparation for EPR analysis. SA and FB have both contributed to the structural analysis. MS and JPD have performed MD simulations and result analyses. SA and JR have performed redox titrations and EPR experiments. Analysis of EPR data was carried-out by JR, SA, SG and BG. The research was conceived, supervised and critically reviewed by AM, JPD, SG and BG. All authors have contributed to the writing of the manuscript.

References

1. Magalon A, Ceccaldi P, Schoepp-Cothenet B. 2017. The prokaryotic Mo/W-bisPGD enzymes superfamily, p 143-191. *In* Hille R, Schulzke C, Kirk ML (ed),

Molybdenum and Tungsten enzymes doi:10.1039/9781782623915−00143 . RCS.
2. Hille R, Hall J, Basu P. 2014. The mononuclear molybdenum enzymes. Chem Rev 114:3963-4038.
3. Ducluzeau AL, van Lis R, Duval S, Schoepp-Cothenet B, Russell MJ, Nitschke W. 2009. Was nitric oxide the first deep electron sink? Trends Biochem Sci 34:9-15.
4. Nitschke W, Russell MJ. 2009. Hydrothermal focusing of chemical and chemiosmotic energy, supported by delivery of catalytic Fe, Ni, Mo/W, Co, S and Se, forced life to emerge. J Mol Evol 69:481-96.
5. Grimaldi S, Schoepp-Cothenet B, Ceccaldi P, Guigliarelli B, Magalon A. 2013. The prokaryotic Mo/W-bisPGD enzymes family: A catalytic workhorse in bioenergetic. Biochim Biophys Acta 1827:1048-85.
6. Magalon A, Fedor JG, Walburger A, Weiner JH. 2011. Molybdenum enzymes in bacteria and their maturation. Coordination Chemistry Reviews 255:1159-1178.
7. Tarrago L, Grosse S, Lemaire D, Faure L, Tribout M, Siponen MI, Kojadinovic-Sirinelli M, Pignol D, Arnoux P, Sabaty M. 2020. Reduction of Protein Bound Methionine Sulfoxide by a Periplasmic Dimethyl Sulfoxide Reductase. Antioxidants (Basel) 9.
8. Wu SY, Rothery RA, Weiner JH. 2015. Pyranopterin Coordination Controls Molybdenum Electrochemistry in *Escherichia coli* Nitrate Reductase. J Biol Chem 290:25164-73.
9. Duval S, Santini JM, Lemaire D, Chaspoul F, Russell MJ, Grimaldi S, Nitschke W, Schoepp-Cothenet B. 2016. The H-bond network surrounding the pyranopterins modulates redox cooperativity in the molybdenum-bisPGD cofactor in arsenite oxidase. Biochim Biophys Acta 1857:1353-1362.
10. Bertero MG, Rothery RA, Palak M, Hou C, Lim D, Blasco F, Weiner JH, Strynadka NC. 2003. Insights into the respiratory electron transfer pathway from the structure of nitrate reductase A. Nat Struct Biol 10:681-7.
11. Jormakka M, Richardson D, Byrne B, Iwata S. 2004. Architecture of NarGH reveals a structural classification of Mo-bisMGD enzymes. Structure 12:95-104.
12. Rothery RA, Bertero MG, Cammack R, Palak M, Blasco F, Strynadka NC, Weiner JH. 2004. The Catalytic Subunit of *Escherichia coli* Nitrate Reductase A Contains a Novel [4Fe-4S] Cluster with a High-Spin Ground State. Biochemistry 43:5324-5333.
13. Schoepp-Cothenet B, van Lis R, Philippot P, Magalon A, Russell MJ, Nitschke W. 2012. The ineluctable requirement for the trans-iron elements molybdenum and/or tungsten in the origin of life. Sci Rep 2:263.
14. Wells M, Kanmanii NJ, Al Zadjali AM, Janecka JE, Basu P, Oremland RS, Stolz JF. 2020. Methane, arsenic, selenium and the origins of the DMSO reductase family. Sci Rep 10:10946.
15. Kloer DP, Hagel C, Heider J, Schulz GE. 2006. Crystal structure of ethylbenzene dehydrogenase from *Aromatoleum aromaticum*. Structure 14:1377-88.
16. Youngblut MD, Tsai CL, Clark IC, Carlson HK, Maglaqui AP, Gau-Pan PS, Redford SA, Wong A, Tainer JA, Coates JD. 2016. Perchlorate Reductase Is Distinguished by Active Site Aromatic Gate Residues. J Biol Chem 291:9190-202.
17. Guigliarelli B, Asso M, More C, Augier V, Blasco F, Pommier J,

Giordano G, Bertrand P. 1992. EPR and redox characterization of iron-sulfur centers in nitrate reductases A and Z from *Escherichia coli*. Evidence for a high-potential and a low-potential class and their relevance in the electron-transfer mechanism. Eur J Biochem 207:61-8.

18. Lanciano P, Savoyant A, Grimaldi S, Magalon A, Guigliarelli B, Bertrand P. 2007. New method for the spin quantitation of [4Fe-4S](+) clusters with S = (3)/(2). Application to the FS0 center of the NarGHI nitrate reductase from *Escherichia coli*. J Phys Chem B 111:13632-7.
19. Magalon A, Asso M, Guigliarelli B, Rothery RA, Bertrand P, Giordano G, Blasco F. 1998. Molybdenum cofactor properties and [Fe-S] cluster coordination in *Escherichia coli* nitrate reductase A: investigation by site-directed mutagenesis of the conserved his-50 residue in the NarG subunit. Biochemistry 37:7363-70.
20. Ceccaldi P, Rendon J, Leger C, Toci R, Guigliarelli B, Magalon A, Grimaldi S, Fourmond V. 2015. Reductive activation of *Escherichia coli* respiratory nitrate reductase. Biochim Biophys Acta 1847:1055-63.
21. Rendon J, Biaso F, Ceccaldi P, Toci R, Seduk F, Magalon A, Guigliarelli B, Grimaldi S. 2017. Elucidating the Structures of the Low- and High-pH Mo(V) Species in Respiratory Nitrate Reductase: A Combined EPR, (14,15)N HYSCORE, and DFT Study. Inorg Chem 56:4423-4435.
22. Hille R. 1996. The Mononuclear Molybdenum Enzymes. Chem Rev 96:2757-2816.
23. Bray RC, Vincent SP, Lowe DJ, Clegg RA, Garland PB. 1976. Electron-paramagnetic-resonance studies on the molybdenum of nitrate reductase from *Escherichia coli* K12. Biochem J 155:201-3.
24. Godfrey C, Greenwood C, Thomson AJ, Bray RC, George GN. 1984. Electron-paramagnetic-resonance spectroscopy studies on the dissimilatory nitrate reductase from *Pseudomonas aeruginosa*. Biochem J 224:601-8.
25. Field SJ, Thornton NP, Anderson LJ, Gates AJ, Reilly A, Jepson BJ, Richardson DJ, George SJ, Cheesman MR, Butt JN. 2005. Reductive activation of nitrate reductases. Dalton Trans doi:10.1039/b505530j:3580-6.
26. Boyington JC, Gladyshev VN, Khangulov SV, Stadtman TC, Sun PD. 1997. Crystal structure of formate dehydrogenase H: catalysis involving Mo, molybdopterin, selenocysteine, and an Fe4S4 cluster. Science 275:1305-8.
27. Czjzek M, Dos Santos JP, Pommier J, Giordano G, Mejean V, Haser R. 1998. Crystal structure of oxidized trimethylamine N-oxide reductase from *Shewanella massilia* at 2.5 A resolution. J Mol Biol 284:435-47.
28. Li H-K, Temple C, Rajagopalan KV, Schindelin H. 2000. The 1.3 A crystal structure of *Rhodobacter sphaeroides* dimethyl sulfoxide reductase reveals two distinct molybdenum coordination environments. J Am Chem Soc 122:7673-7680.
29. Arnoux P, Sabaty M, Alric J, Frangioni B, Guigliarelli B, Adriano JM, Pignol D. 2003. Structural and redox plasticity in the heterodimeric periplasmic nitrate reductase. Nat Struct Biol 10:928-34.
30. Ellis PJ, Conrads T, Hille R, Kuhn P. 2001. Crystal structure of the 100 kDa arsenite oxidase from *Alcaligenes faecalis* in two crystal forms at 1.64 A and 2.03 A. Structure 9:125-32.
31. Messerschmidt A, Niessen H, Abt D, Einsle O, Schink B, Kroneck

PM. 2004. Crystal structure of pyrogallol-phloroglucinol transhydroxylase, an Mo enzyme capable of intermolecular hydroxyl transfer between phenols. Proc Natl Acad Sci U S A 101:11571-6.

32. Seiffert GB, Ullmann GM, Messerschmidt A, Schink B, Kroneck PM, Einsle O. 2007. Structure of the non-redox-active tungsten/[4Fe:4S] enzyme acetylene hydratase. Proc Natl Acad Sci U S A 104:3073-7.
33. Jormakka M, Yokoyama K, Yano T, Tamakoshi M, Akimoto S, Shimamura T, Curmi P, Iwata S. 2008. Molecular mechanism of energy conservation in polysulfide respiration. Nat Struct Mol Biol 15:730-7.
34. Coelho C, Gonzalez PJ, Moura JG, Moura I, Trincao J, Joao Romao M. 2011. The crystal structure of *Cupriavidus necator* nitrate reductase in oxidized and partially reduced states. J Mol Biol 408:932-48.
35. Wagner T, Ermler U, Shima S. 2016. The methanogenic CO2 reducing-and-fixing enzyme is bifunctional and contains 46 [4Fe-4S] clusters. Science 354:114-117.
36. Radon C, Mittelstadt G, Duffus BR, Burger J, Hartmann T, Mielke T, Teutloff C, Leimkuhler S, Wendler P. 2020. Cryo-EM structures reveal intricate Fe-S cluster arrangement and charging in *Rhodobacter capsulatus* formate dehydrogenase. Nat Commun 11:1912.
37. Oliveira AR, Mota C, Mourato C, Domingos RM, Santos MFA, Gesto D, Guigliarelli B, Santos-Silva T, Romao MJ, Pereira IAC. 2020. Toward the Mechanistic Understanding of Enzymatic CO2 Reduction. ACS Catalysis 10:3844-3856.
38. Liebgott PP, Leroux F, Burlat B, Dementin S, Baffert C, Lautier T, Fourmond V, Ceccaldi P, Cavazza C, Meynial-Salles I, Soucaille P, Fontecilla-Camps JC, Guigliarelli B, Bertrand P, Rousset M, Leger C. 2010. Relating diffusion along the substrate tunnel and oxygen sensitivity in hydrogenase. Nat Chem Biol 6:63-70.
39. Liebgott PP, de Lacey AL, Burlat B, Cournac L, Richaud P, Brugna M, Fernandez VM, Guigliarelli B, Rousset M, Leger C, Dementin S. 2011. Original design of an oxygen-tolerant [NiFe] hydrogenase: major effect of a valine-to-cysteine mutation near the active site. J Am Chem Soc 133:986-97.
40. Marques S, Brezovsky J, Damborsky J. 2016. Role of tunnels and gates in enzymatic catalysis, p 421-463, Understanding enzymes. Pan Stanford.
41. Oprea TI, Hummer G, Garcia AE. 1997. Identification of a functional water channel in cytochrome P450 enzymes. Proc Natl Acad Sci U S A 94:2133-8.
42. Holm RH, Kennepohl P, Solomon EI. 1996. Structural and Functional Aspects of Metal Sites in Biology. Chem Rev 96:2239-2314.
43. Biedermannova L, Prokop Z, Gora A, Chovancova E, Kovacs M, Damborsky J, Wade RC. 2012. A single mutation in a tunnel to the active site changes the mechanism and kinetics of product release in haloalkane dehalogenase LinB. J Biol Chem 287:29062-74.
44. Cojocaru V, Winn PJ, Wade RC. 2007. The ins and outs of cytochrome P450s. Biochim Biophys Acta 1770:390-401.
45. Winkler M, Duan J, Rutz A, Felbek C, Scholtysek L, Lampret O, Jaenecke J, Apfel UP, Gilardi G, Valetti F, Fourmond V, Hofmann E, Leger C, Happe T. 2021. A safety cap protects hydrogenase from oxygen attack. Nat Commun 12:756.

46. Chovancova E, Pavelka A, Benes P, Strnad O, Brezovsky J, Kozlikova B, Gora A, Sustr V, Klvana M, Medek P, Biedermannova L, Sochor J, Damborsky J. 2012. CAVER 3.0: a tool for the analysis of transport pathways in dynamic protein structures. PLoS Comput Biol 8:e1002708.
47. Lanciano P, Vergnes A, Grimaldi S, Guigliarelli B, Magalon A. 2007. Biogenesis of a respiratory complex is orchestrated by a single accessory protein. J Biol Chem 282:17468-74.
48. Lowry OH, Rosebrough NJ, Farr AL, Randall RJ. 1951. Protein measurement with the Folin phenol reagent. J Biol Chem 193:265-75.
49. Arnoux P, Ruppelt C, Oudouhou F, Lavergne J, Siponen MI, Toci R, Mendel RR, Bittner F, Pignol D, Magalon A, Walburger A. 2015. Sulphur shuttling across a chaperone during molybdenum cofactor maturation. Nat Commun 6:6148.
50. Morpeth FF, Boxer DH. 1985. Kinetic analysis of respiratory nitrate reductase from *Escherichia coli* K12. Biochemistry 24:40-6.
51. Buc J, Santini CL, Blasco F, Giordani R, Cardenas ML, Chippaux M, Cornish-Bowden A, Giordano G. 1995. Kinetic studies of a soluble alpha beta complex of nitrate reductase A from *Escherichia coli*. Use of various alpha beta mutants with altered beta subunits. Eur J Biochem 234:766-72.
52. Giordani R, Buc J, Cornish-Bowden A, Cardenas ML. 1997. Kinetics of membrane-bound nitrate reductase A from *Escherichia coli* with analogues of physiological electron donors--different reaction sites for menadiol and duroquinol. Eur J Biochem 250:567-77.
53. Wilkinson AJ, Fersht AR, Blow DM, Winter G. 1983. Site-directed mutagenesis as a probe of enzyme structure and catalysis: tyrosyl-tRNA synthetase cysteine-35 to glycine-35 mutation. Biochemistry 22:3581-6.
54. Stoll S, Schweiger A. 2006. EasySpin, a comprehensive software package for spectral simulation and analysis in EPR. J Magn Reson 178:42-55.
55. Cornell WD, Cieplak P, Bayly CI, Gould IR, Merz KM, Ferguson DM, Spellmeyer DC, Fox T, Caldwell JW, Kollman PA. 1995. A Second Generation Force Field for the Simulation of Proteins, Nucleic Acids, and Organic Molecules. Journal of the American Chemical Society 117:5179-5197.
56. Smith DM, Xiong Y, Straatsma TP, Rosso KM, Squier TC. 2012. Force-Field Development and Molecular Dynamics of [NiFe] Hydrogenase. J Chem Theory Comput 8:2103-14.
57. Meagher KL, Redman LT, Carlson HA. 2003. Development of polyphosphate parameters for use with the AMBER force field. Journal of Computational Chemistry 24:1016-1025.
58. Rostkowski M, Olsson MH, Sondergaard CR, Jensen JH. 2011. Graphical analysis of pH-dependent properties of proteins predicted using PROPKA. BMC Struct Biol 11:6.
59. Berendsen HJC, Van der Spoel D, Van Drunen R. 1995. GROMACS: A message-passing parallel molecular dynamics implementation. Computer Physics Communications 91:43-56.
60. Hess B, Kutzner C, Van der Spoel D, Lindahl E. 2008. GROMACS 4: Algorithms for Highly Efficient, Load-Balanced, and Scalable Molecular Simulation. Journal of Chemical Theory and Computation 4:435-447.
61. Lindahl E, Hess B, Van der Spoel D. 2001. GROMACS 3.0: a package for molecular simulation and

trajectory analysis. Molecular modeling annual 7:306-317.
62. Van der Spoel D, Lindahl E, Hess B, Groenhof G, Mark AE, Berendsen HJC. 2005. GROMACS: fast, flexible, and free. Journal of Computational Chemistry 103:8577-8593.
63. Essmann U, Perera L, Berkowitz ML, Darden TA, Lee HI, Pedersen LG. 1995. A smooth particle mesh Ewald method. The Journal of Chemical Physics 103:8577-8593.
64. Bussi G, Donadio D, Parrinello M. 2007. Canonical sampling through velocity rescaling. Journal of Chemical Physics 126:014101.
65. Parrinello M, Rahman A. 1981. Polymorphic transitions in single crystals: A new molecular dynamics method. Journal of Applied Physics 52:7182-7190.
66. Humphrey W, Dalke A, Schulten K. 1996. VMD: visual molecular dynamics. Journal of Molecular Graphics 14:27-38.
67. Dementin S, Burlat B, De Lacey AL, Pardo A, Adryanczyk-Perrier G, Guigliarelli B, Fernandez VM, Rousset M. 2004. A glutamate is the essential proton transfer gate during the catalytic cycle of the [NiFe] hydrogenase. J Biol Chem 279:10508-13.
68. Ravichandran K, Minnihan EC, Lin Q, Yokoyama K, Taguchi AT, Shao J, Nocera DG, Stubbe J. 2017. Glutamate 350 Plays an Essential Role in Conformational Gating of Long-Range Radical Transport in *Escherichia coli* Class Ia Ribonucleotide Reductase. Biochemistry 56:856-868.
69. Harris TK, Turner GJ. 2002. Structural basis of perturbed pKa values of catalytic groups in enzyme active sites. IUBMB Life 53:85-98.
70. Cornish-Bowden A. 2004. Fundamentals of enzyme kinetics. Portland Press Ltd., London.
71. Grimaldi S, Biaso F, Burlat B, Guigliarelli B. 2017. Electron Paramagnetic Resonance Studies of Molybdenum Enzymes, p 68-120. *In* Hille R, Schulzke C, Kirk ML (ed), Molybdenum and Tungsten enzymes. RCS.
72. Butler CS, Fairhurst SA, Ferguson SJ, Thomson AJ, Berks BC, Richardson DJ, Lowe DJ. 2002. Mo(V) co-ordination in the periplasmic nitrate reductase from *Paracoccus pantotrophus* probed by electron nuclear double resonance (ENDOR) spectroscopy. Biochem J 363:817-823.
73. Fourmond V, Burlat B, Dementin S, Arnoux P, Sabaty M, Boiry S, Guigliarelli B, Bertrand P, Pignol D, Leger C. 2008. Major Mo(V) EPR signature of *Rhodobacter sphaeroides* periplasmic nitrate reductase arising from a dead-end species that activates upon reduction. Relation to other molybdoenzymes from the DMSO reductase family. J Phys Chem B 112:15478-86.
74. Zeamari K, Gerbaud G, Grosse S, Fourmond V, Chaspoul F, Biaso F, Arnoux P, Sabaty M, Pignol D, Guigliarelli B, Burlat B. 2019. Tuning the redox properties of a [4Fe-4S] center to modulate the activity of Mo-bisPGD periplasmic nitrate reductase. Biochim Biophys Acta Bioenerg 1860:402-413.
75. Vincent SP, Bray RC. 1978. Electron-paramagnetic-resonance studies on nitrate reductase from *Escherichia coli* K12. Biochem J 171:639-47.
76. Latimer WM, Rodebush WH. 1920. Polarity and ionization from the standpoint of the Lewis theory of valence. Journal of the American Chemical Society 42:1419-1433.
77. Agmon N. 1995. The Grotthuss mechanism. Chemical Physics letters 244:456-462.

78. Gora A, Brezovsky J, Damborsky J. 2013. Gates of enzymes. Chem Rev 113:5871-923.
79. Volbeda A, Martin L, Cavazza C, Matho M, Faber BW, Roseboom W, Albracht SP, Garcin E, Rousset M, Fontecilla-Camps JC. 2005. Structural differences between the ready and unready oxidized states of [NiFe] hydrogenases. J Biol Inorg Chem 10:239-49.
80. Kaila VR, Wikstrom M, Hummer G. 2014. Electrostatics, hydration, and proton transfer dynamics in the membrane domain of respiratory complex I. Proc Natl Acad Sci U S A 111:6988-93.
81. Clark IC, Melnyk RA, Engelbrektson A, Coates JD. 2013. Structure and evolution of chlorate reduction composite transposons. mBio 4.
82. Dias JM, Than ME, Humm A, Huber R, Bourenkov GP, Bartunik HD, Bursakov S, Calvete J, Caldeira J, Carneiro C, Moura JJ, Moura I, Romao MJ. 1999. Crystal structure of the first dissimilatory nitrate reductase at 1.9 A solved by MAD methods. Structure Fold Des 7:65-79.
83. Jepson BJ, Mohan S, Clarke TA, Gates AJ, Cole JA, Butler CS, Butt JN, Hemmings AM, Richardson DJ. 2007. Spectropotentiometric and structural analysis of the periplasmic nitrate reductase from *Escherichia coli*. J Biol Chem 282:6425-37.
84. Hettmann T, Siddiqui RA, Frey C, Santos-Silva T, Romao MJ, Diekmann S. 2004. Mutagenesis study on amino acids around the molybdenum centre of the periplasmic nitrate reductase from *Ralstonia eutropha*. Biochem Biophys Res Commun 320:1211-9.
85. Dementin S, Arnoux P, Frangioni B, Grosse S, Leger C, Burlat B, Guigliarelli B, Sabaty M, Pignol D. 2007. Access to the active site of periplasmic nitrate reductase: insights from site-directed mutagenesis and zinc inhibition studies. Biochemistry 46:9713-21.
86. Wang TH, Chen YH, Huang JY, Liu KC, Ke SC, Chu HA. 2011. Enzyme kinetics, inhibitors, mutagenesis and electron paramagnetic resonance analysis of dual-affinity nitrate reductase in unicellular N(2)-fixing cyanobacterium *Cyanothece* sp. PCC 8801. Plant Physiol Biochem 49:1369-76.
87. Srivastava AP, Allen JP, Vaccaro BJ, Hirasawa M, Alkul S, Johnson MK, Knaff DB. 2015. Identification of Amino Acids at the Catalytic Site of a Ferredoxin-Dependent Cyanobacterial Nitrate Reductase. Biochemistry 54:5557-68.
88. Haapanen O, Sharma V. 2017. Role of water and protein dynamics in proton pumping by respiratory complex I. Sci Rep 7:7747.
89. Muhlbauer ME, Saura P, Nuber F, Di Luca A, Friedrich T, Kaila VRI. 2020. Water-Gated Proton Transfer Dynamics in Respiratory Complex I. J Am Chem Soc 142:13718-13728.
90. Khaniya U, Gupta C, Cai X, Mao J, Kaur D, Zhang Y, Singharoy A, Gunner MR. 2020. Hydrogen bond network analysis reveals the pathway for the proton transfer in the E-channel of *Thermus thermophilus* Complex I. Biochim Biophys Acta Bioenerg 1861:148240.